World Journal of Engineering and Technology, 2025, 13(4),1053-1066
https://www.scirp.org/journal/wjet
ISSN Online: 2331-4249
ISSN Print: 2331-4222

Molecular Dynamics Simulation of Deformation of FCC Bicrystal Nanopillars under Compression

Takuya Uehara[1*], Yuki Shigihara[2]

[1]Department of Mechanical Systems Engineering, Yamagata University, Yonezawa, Japan
[2]Graduate School of Engineering and Science, Yamagata University, Yonezawa, Japan
Email: *uehara@yz.yamagata-u.ac.jp

How to cite this paper: Uehara, T. and Shigihara, Y. (2025) Molecular Dynamics Simulation of Deformation of FCC Bicrystal Nanopillars under Compression. *World Journal of Engineering and Technology*, **13**, 1053-1066.
https://doi.org/10.4236/wjet.2025.134063

Received: September 21, 2025
Accepted: November 17, 2025
Published: November 20, 2025

Copyright © 2025 by author(s) and Scientific Research Publishing Inc.
This work is licensed under the Creative Commons Attribution International License (CC BY 4.0).
http://creativecommons.org/licenses/by/4.0/
Open Access

Abstract

Nanopillars have attracted considerable attention in nanoengineering because of their superior optical, chemical, and biological properties, which have led to their use in nanodevices and various applications. From the viewpoint of mechanics of materials, nanopillars are also good specimens for investigating the deformation mechanism of crystalline materials. In this study, molecular dynamics simulations were performed to evaluate the compressive deformation of nanopillars. Bicrystal models were used to focus on the effect of grain boundaries on the deformation mechanism. Two types of models were developed; the grain boundary was set parallel or perpendicular to the loading direction along the longitudinal axis of the pillar. When the grain boundary was parallel to the axis, slip occurred in each crystal independently, and the grain boundary separated the motion of dislocation via compression. In contrast, when the boundary was perpendicular to the axis, plastic deformation proceeded in one of the crystals, and the grain boundary separated the deformed and undeformed regions.

Keywords

Molecular Dynamics, Computer Simulation, Nanopillar, Deformation Mechanism, Crystalline Material, Slip, Dislocation

1. Introduction

Nanopillars are small columnar specimens or parts of devices on a nanometer scale and have attracted considerable attention in nanoengineering because of their superior optical, chemical, medical, and biological properties. For example,

a solar panel device with a nanopillar-based nanostructure exhibits high performance because of its large surface area, and a dragonfly wing with a nanopillar structure exhibits high water repellency and low air resistance. Due to the recent advancement in nano-technology, these structures have been applied to various products with specific performance in antibacterial properties, photovoltaic function, and so on [1]-[5]. In addition to these practical applications, nanopillars serve as good specimens for clarifying the deformation mechanism of crystalline materials such as metals, alloys, ceramics, and composites. Plastic deformation in metals is preceded by the slip behavior of certain crystal planes caused by the generation and motion of dislocations. Because such atomistic behavior occurs inside the material, a direct observation is difficult. Furthermore, typical experimental specimens are subject to various restrictions, making it challenging to achieve natural behavior without any constraints. Nanopillars, being very small and thin, allow almost restriction-free conditions. However, because grabbing nanopillars for tensile testing is problematic, compression tests are most commonly used to investigate their mechanical properties. Scanning electron microscopy (SEM) images of micropillars (100 nm - 10 nm) [6]-[8] revealed multiple steps on the side surfaces, which are caused by slip on specific planes such as {111} planes in face-centered cubic (FCC) metals [9] [10]. Although these results indicate the occurrence of a slip mechanism, direct observation during the deforming process on a nanometer scale remains difficult. Therefore, computer simulations are more suitable for clarifying the dynamic behavior of material deformation. In this sense, the molecular dynamics (MD) method is a powerful tool that enables direct simulation of the atomistic dynamic process. So far, various models have been reported for micro or nanopillars, and the target materials include pure metals, two-component alloys, and complex multi-component alloys [11]-[16]. Regarding the plastic deformation mechanism, the crystallographic orientation plays a critical role. Thus, even for single-crystalline models, an infinite number of variations in the relation between the crystal orientation and loading direction exist. In addition, the role of grain boundaries (GB) is the key to clarifying the mechanism of plastic deformation in polycrystalline materials. In this regard, various studies have been conducted. Despite extensive research, however, a comprehensive understanding of the mechanism is still lacking. Addressing this issue requires the accumulation of simulation data on various cases.

In this study, MD simulations were demonstrated for the compressive deformation of nanopillars using bicrystal models. Two types of models were prepared [17]; the GB was set parallel or perpendicular to the loading direction. Various orientation combinations were applied for each model, and the deformation mechanism and the GB effects were discussed.

2. Simulation Models and Conditions

2.1. Nanopillar Models

In this study, an FCC metal was considered. **Figure 1(a)** shows a single-crystalline

pillar of a square cross-section. The cubic unit cells of the FCC crystal were arranged along the *x*-, *y*-, and *z* axes giving the size of approximately 7.2 nm × 7.2 nm × 21.7 nm. The crystallographic orientation is (001) on the *x*-*y* plane and [100] along the x-axis. Figure 1(b) shows the atomic configuration of a unit cell of the FCC crystal and the representative {111} planes, which are expected to be the slip plane. The orientation was varied by rotating the (100) plane around the x-axis. An example of a 45˚ rotated model is shown in Figure 1(c), in which the slip plane is parallel to the y-axis and inclined 45˚ from both the x- and z-axes. In addition to the pillar parts, fix plates were set on the top and bottom faces. These plates were constructed from the FCC crystal and connected to the pillar atoms via interatomic interactions; however, their dynamic motion was not calculated. The top plate was moved downward at a constant rate during the loading process.

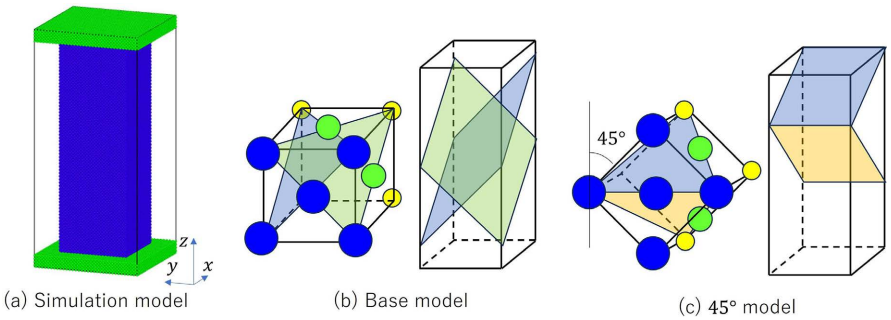

Figure 1. Illustration of a nanopillar model (a), orientation of base model (b), and 45˚ model (c) with typical slip {111} planes in each model.

2.2. Bicrystal Models

Two types of bicrystal models were prepared. In the vertical GB model, the pillar was divided in two regions separated by the central vertical plane parallel to the y-z plane, as shown in Figure 2(a). The atoms in each domain were rotated by angles q_i around the *y*-axis, where *i* denotes the domain number, 1 or 2 for the left and right domain, respectively. The angle is measured from the z axis, as shown in Figure 2(a), and symmetric GB models are generated when $\theta_1 = \theta_2$. In this study, asymmetric GB for $\theta_1 = 0$ and $\theta_2 \neq 0$ was also investigated. In this paper, the models are referred to as Vθ_1-θ_2 model. Another model is the horizontal GB model, as shown in Figure 2(b). In this model, the boundary of the two domain is set parallel to the x-y plane and perpendicular to the loading direction. The crystal in each domain was rotated in the same way as the vertical GB model, and symmetric or asymmetric GB was prepared. These are referred to as Lθ_1-θ_2 model.

Simulations were demonstrated for many combinations of θ_1 and θ_2, though typical results are shown in this paper.

2.3. Loading Conditions

A compression load was imposed by moving the top plate downward at a constant

rate $v = 0.005$ nm/ps with the time increment $\Delta t = 0.01$ ps/timestep. The interaction between the atoms in the plate and the pillar was governed by the interatomic forces, while no external forces were applied to restrict the sliding or friction. The temperature was controlled at $T = 1$ K using the Nose-Hoover method to avoid thermal effects.

2.4. Simulation Tool

The simulations were performed using LAMMPS [18]. The interatomic interaction was assumed to be expressed by the embedded-atom-method (EAM) potential function for Cu proposed by Zhou *et al.* [19]. The results were visualized using OVITO [20]. Common-neighbor analysis (CNA) [21] and the centrosymmetric parameter (CSP) [22] are often applied for identifying the crystal structure and local characteristics around the atoms. In this study, the CNA results are used to visualize the atomic configuration by coloring the atoms. This method is effective because hexagonal closed-packed (HCP) layers indicate stacking faults or a partial-dislocation plane within the FCC crystals, thereby revealing the front position of the deformed zone.

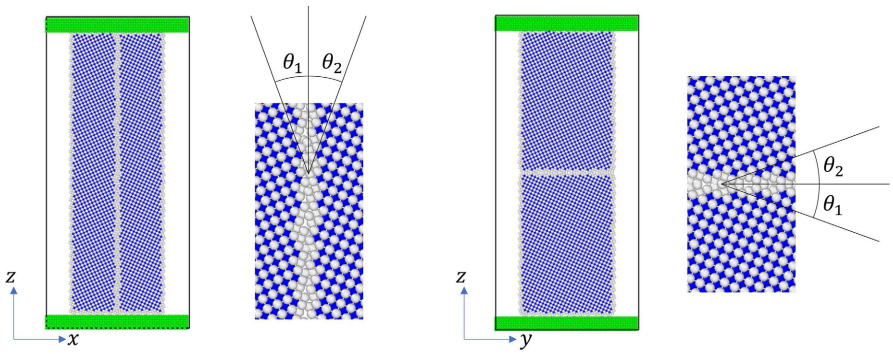

Figure 2. Bicrystal models with the rotation angle in each model.

3. Results for Single-Crystal Models

Before simulating the bicrystal models, the simulation method and conditions were verified using single-crystal models. Differently oriented models were developed by applying rotations of angles θ around the y-axis. Figure 3 shows variations in the atomic configuration during compression for the $\theta = 0$ model. The visualization uses a color scheme based on the CNA results, where FCC atoms are shown in blue, HCP atoms in red, body-centered cubic (BCC) atoms in yellow, and atoms with other coordination structures in gray. Note that the atoms on the surface and GB are depicted in gray, and BCC atoms appear only temporarily. Therefore, the notable phenomenon is the appearance of HCP atoms in the FCC crystal. Following the initial elastic deformation, an oblique line appeared at the 35,000th timestep. The origin of this line was the top-left corner contacting the top plate, and the HCP atoms are spreading inside the pillar and forming an HCP

layer. The first layer traversed the model and another HCP layer appeared by the 36,000th timestep (Figure 3(b)). The region between the two HCP layers is FCC structure, though the orientation is different from the other region. The HCP layer was determined as the HCP structure by the CNA analysis; however, it represents a stacking fault or a partial dislocation layer. A pair of HCP layers was parallel to each other, and they widened the distance as compression progressed (Figures 3(c)-(f)). At the same time, other HCP layers on one of the equivalent {111} plane were also generated. They tended to propagate but interfered at the initial HCP layer, and the firstly formed deformation zone primarily developed.

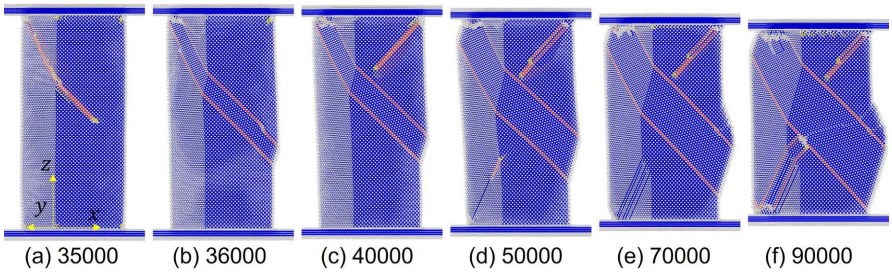

Figure 3. Atomic configuration under compression for 0˚ single-crystal model from the 35,000th to 90,000th timesteps colored by CNA indicator, where blue indicates FCC atoms, red indicates HCP atoms, and gray indicates other atoms.

Figure 4 presents the simulation results obtained for the 45˚ model under the same conditions. The {111} slip plane appeared as a 45˚ line on the side face at the 26,000th timestep, as shown in Figure 4(a). It appeared to initiate at the boundary between the pillar and upper plate and was reflected at the back surface. Consequently, another 45˚ slip occurred at the front by the 27,000th timestep (Figure 4(b)). Other slips occurred subsequently, and several steps appeared on the front surface.

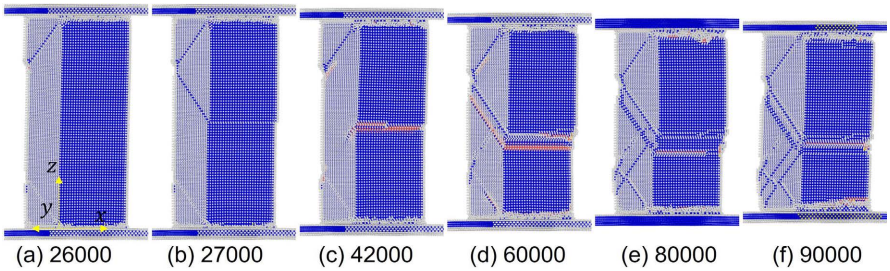

Figure 4. Atomic configuration under compression for 45˚ single-crystal model from the 26,000th to 90,000th timesteps colored by CNA indicator.

The stress variations for these models are shown in Figure 5. It should be noted that this diagram is equivalent to the stress-strain relation, because the compressive displacement is applied at a constant rate. A significant difference in the initial slope corresponds to the anisotropic elastic modulus, and the sudden drops correspond to the initiation of the slip observed in Figure 3 and Figure 4. Significant

differences were observed not only in elasticity and plastic flow stress but also in the ease of slip deformation.

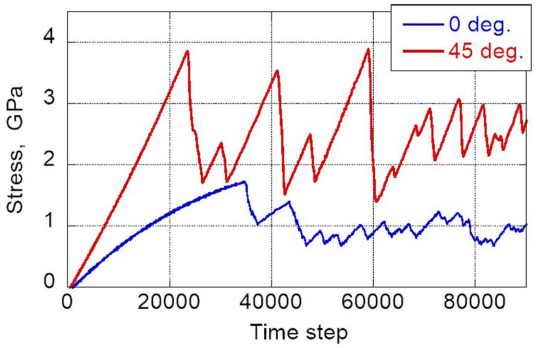

Figure 5. Variation of the compressive stress for 0˚ and 45˚ single-crystal models.

These results are reasonable compared with previously reported results, confirming that the present model and method can be applied to further studies using bicrystal models.

4. Vertical GB Bicrystals

4.1. Representative Results

Figure 6 shows the result for the vertical asymmetric GB model with $\theta_1 = 0^\circ$ and $\theta_2 = 45^\circ$ (V0-45 model). The coloring in **Figure 6(a)** corresponds to the CNA result, using the same scheme as in **Figure 3**. **Figure 6(b)** shows only the HCP layers. The slip first occurred in the right-hand-side region of $\theta_2 = 45^\circ$ at the 20,000th timestep, where the {111} plane appeared as a horizontal line parallel to the x-axis on the front surface, as illustrated in **Figure 1(a)**. Subsequently, the second slip was observed in the left-hand-side region, where the {111} plane was arranged in an oblique rhombus shape, as illustrated in **Figure 1(b)**. Thereafter, slip behaviors were observed in both regions independently, maintaining the vertical GB at the original position. The final shape shows apparent 45° steps on the side surface resulting from the {111} slip, as shown in **Figure 6(a)(vi)**, which is shown at an oblique angle.

The stress variation is shown in **Figure 6(c)**. The elastic modulus of the bicrystal nanopillar (green curve) lies between those of the single-crystalline nanopillars (red and blue), but is closer to that of the harder 45° curve. The elastic limit, which corresponds to the initiation of the slip, is expressed by the sudden drop in stress. Although the stress at this point lies between those of single crystals, it occurs earlier than in either. The disordered configuration at the GB is considered to act as the initiation point for the slip. The drop in stress at the elastic limit is not as significant as that in single crystals but continues toward the plastic flow, owing to the intermittent generation of slip planes, as shown in **Figures 6(a)(iii)-(a)(vi)**.

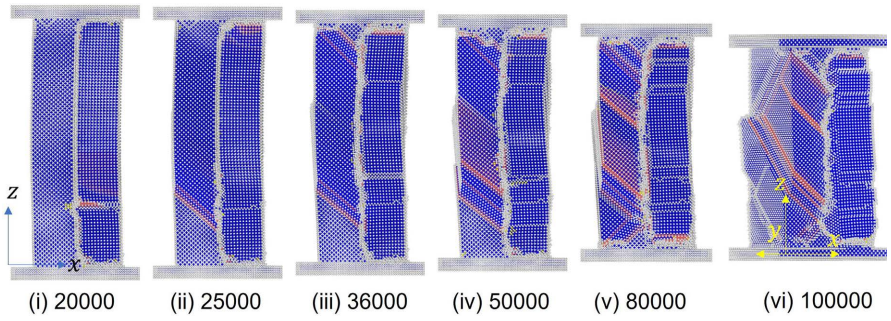

(a) Variations in atomic configuration

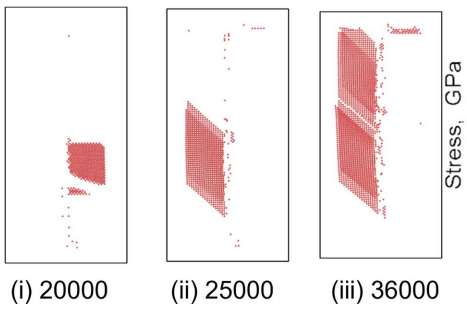

(b) Transparent view of HCP

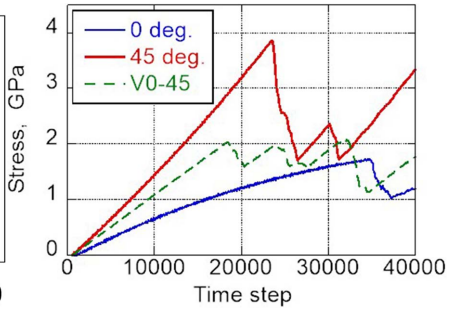

(c) Stress variation

Figure 6. Atomic configuration under compression colored by CNA indicator (a), view of HCP layers (b), and stress variation (c) for asymmetric V0-45 model.

4.2. Various Results by Other Models

Various combinations of crystal orientations were investigated, and two representative cases are presented. Figure 7 shows the result for the symmetric 10˚ - 10˚ model (V10-10). Before starting the compression, a relaxation calculation was performed every time. After this relaxation period, the GB appeared as consecutive dislocations, as shown in Figure 7(a), where the dislocations are perpendicular to the surface and appear as discrete dots. A slip plane was generated from one of these dislocations and spread on the {111} plane. When the slip transmitted across the crystal and propagated through the surface, the misorientation was resolved, and the GB disappeared in exchange for the generation of steps on the surface, as shown in Figures 7(b)-(f). Similar tendencies have been commonly observed for most models with low-angle GBs.

Another typical case is shown in Figure 8, which presents the results for the symmetric V20-20 model. The first slip was observed at the 16,000th timestep in the left-hand-side grain, as shown in Figure 8(a). Subsequently, another slip plane was observed in the symmetric region on the left-hand side (Figure 8(b)). Then, the slip propagated on the right-hand side (Figure 8(c)), followed by the left-hand side (Figure 8(d)). The slip alternated between the two sides, allowing the overall compression to continue while keeping balance. Consequently, the vertical GB maintained a roughly straight configuration, and the overall pillar retained a rectangular shape.

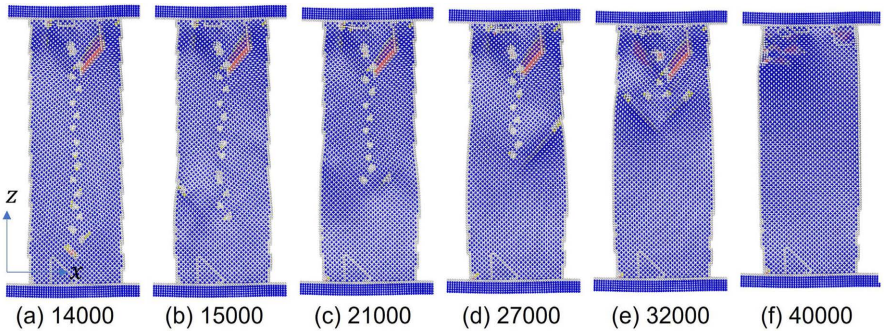

Figure 7. Atomic configuration under compression for symmetric V10-10 model from the 16,000th to 100,000th timesteps colored by CNA indicator.

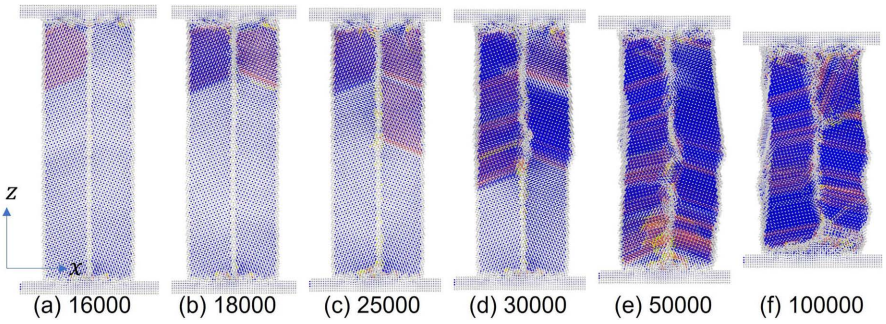

Figure 8. Atomic configuration under compression for symmetric V20-20 model from the 16,000th to 100,000th timesteps colored by CNA indicator.

Figure 9 shows the stress variations for various vertical symmetric GB models. The difference in the initial slope corresponds to the anisotropy in elasticity. The stress curve for the V5-5 model shows minor drops in the elastic curve and major drops around the 15,000th and 20,000th timesteps. Figure 7 shows that the dislocations at the original GB diminish at these times. In the stress curve for the V50-50 model, the initial elastic curve is nearly linear; however, the slope decreased at around the 12,000th timestep before the drastic drop at the 18,000th timestep. Figure 10 illustrates the change in the atomic configuration. The first HCP layer appeared at the 12,000th timestep. The slip plane had nearly the same orientation as that of the 45˚ model (see Figure 1(c)), forming an approximately 45˚ line on the side face. This corresponds to the onset of the decline in the elastic slope. Subsequently, similar alternating slips occur between the left-hand and right-hand sides before the 18,000th timestep. Then, one of the HCP layers, or the stacking fault of the FCC crystal, completely traversed the crystal, thereby generating an apparent step on the side surface at the 18,000th timestep. This is the point of the drastic stress drop observed in Figure 9.

5. Lateral GB Bicrystals

5.1. Representative Results

Following the vertical GB models in the previous section, lateral GB models were investigated. Figure 11 shows the results for the L0-45 model, where the

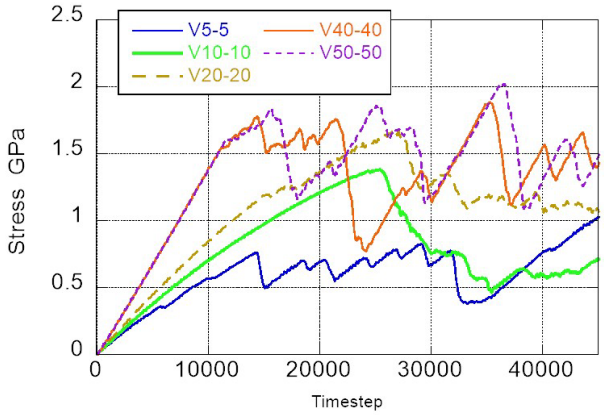

Figure 9. Stress variation for vertical symmetric grain-boundary models.

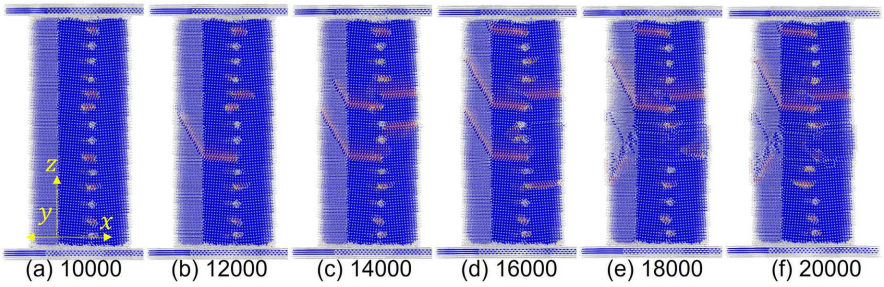

Figure 10. Atomic configuration under compression for symmetric V50-50 bicrystal model from the 10,000th to 20,000th timesteps colored by CNA indicator.

lower-half region has a 45˚ rotated orientation. The slip occurs in the upper-half region on the (111) plane, as shown in **Figure 11(a)**. The slip region spreads in the upper-half grain. After the first HCP layer traverses from the GB to the surface, another HCP layer parallel to the first layer moves upward, maintaining the parallel relation (**Figures 11(a)-(c)**). The motion stops when the upper edge reaches a top plate. The zone between the two HCP layers persists in the FCC structure; however, the orientation is changed. As explained in Section 3, the region between the layers has a different orientation, and an oblique plane appears on the surface. In this model, the GB at the middle pillar also changes the angle. Finally, the upper-half region of the pillar deforms significantly, and the original rectangular shape is no longer maintained. Many slips were observed in the pillar but all of them were in the upper grain, except one slip generated after the 100,000th timestep.

Similar tendencies were observed for other models at various angles in the upper-half region. An example of the L0-40 model is shown in **Figure 12**. The angle of the HCP layer is different according to the crystal orientation; however, significant deformation occurs in the upper region. **Figure 12(b)** shows the HCP layers in the pillar by erasing all atoms except the HCP atoms. The slips are concentrated in the upper-half region. **Figure 12(c)** shows the cross-section of the pillar at the middle plane in the *x*-axis. The upper-half grain is divided into

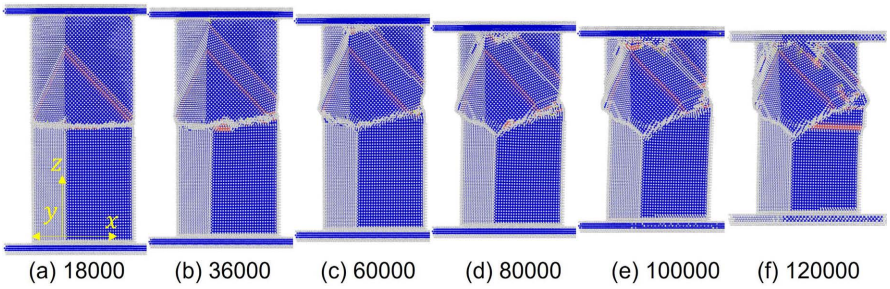

Figure 11. Atomic configuration under compression for lateral asymmetric L0-45 model from the 18,000th to 120,000th timesteps colored by CNA indicator.

several sub-grains with different orientations, where the HCP layers are the boundaries, whereas an almost perfect crystal state is maintained in the lower-half region.

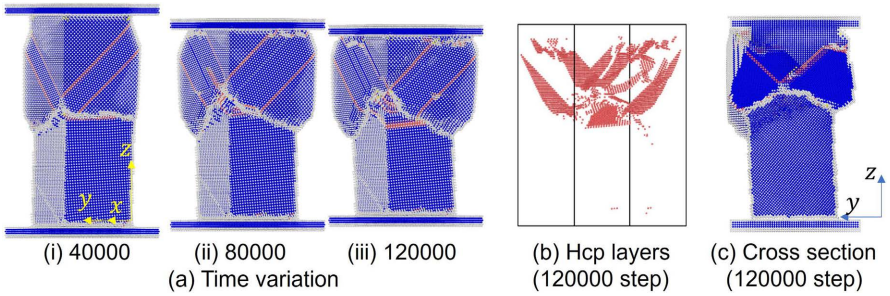

Figure 12. Atomic configuration under compression for lateral asymmetric L0-40 model: (a) time variation, (b) HCP layers, and (c) cross-section at $x = 0.5L_x$.

5.2. Various Results by Other Models

Symmetric bicrystals with lateral GBs were also simulated. The results revealed to be divided into two types. The first type is shown in Figure 13, which presents the result for the L20-20 model. The upper and lower regions have symmetric orientations; thus, the slip lines are also generated symmetrically, as is the case with the vertical symmetric models, as described in Section 4.2 and shown in Figure 8. In this case, the first slip occurs in the upper crystal at the 24,000th timestep (Figure 13(a)), followed by the second slip in the lower crystal (Figure 13(b)). Each slip propagates within its region, and additional slip planes are generated successively. As the slip plane traverses the region to the surface, the side face becomes partially oblique according to the {111} plane, and the pillar bends into an elbow shape, as shown in Figure 13(f). The GB maintains its central position and flat shape despite the significant deformation.

Another typical case is shown in Figure 14, which presents the result for the L60-60 model. The initiation of the first HCP layer appears identical to the previous case. However, although an HCP layer is generated in the upper region from the central GB to the left surface, a pair of parallel layers is not generated. Therefore, no sandwiched FCC region or bent surfaces form between the two HCP layers. Instead, an apparent or macroscopic sliding occurs on the firstly generated

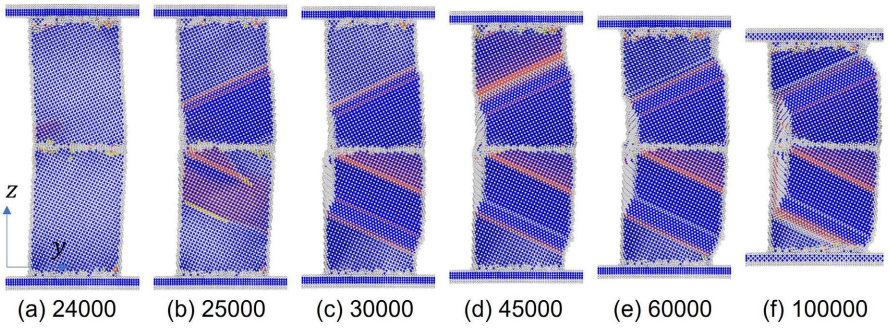

Figure 13. Atomic configuration under compression for lateral symmetric L20-20 bicrystal model from the 24,000th to 100,000th timesteps colored by CNA indicator.

HCP layer. The crystal orientations of both the upper and lower crystals are maintained, keeping the side faces perpendicular. Consequently, the upper and lower crystals slide on the 45˚ plane, and the axes are misaligned. The compressive deformation progressed as the slide distance increased, while the original crystal orientations were preserved.

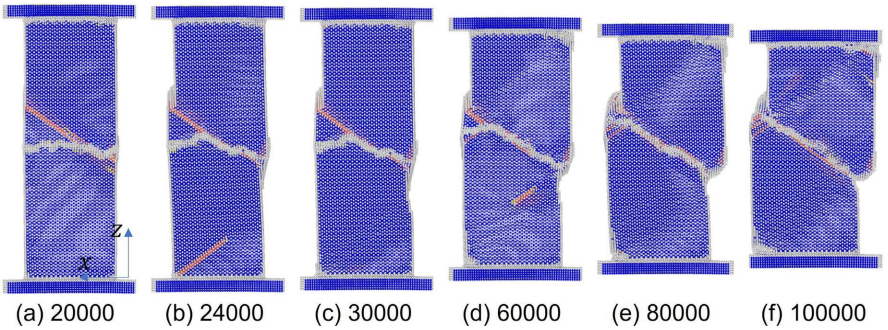

Figure 14. Atomic configuration under compression for lateral symmetric L60-60 model from the 20,000th to 100,000th timesteps colored by CNA indicator.

Figure 15 presents the result for the L70-70 model. Although the result is mostly identical to that of the L20-20 model, it reveals that the deformation is not always symmetrical. In this case, differently oriented slips are observed in the lower region, and the central GB does not maintain a flat shape. The {111} slip plane in the FCC crystal has eight equivalent directions, and the active plane is typically determined by the Schmid factor. As the deformation progressed, the orientation slightly varied, and the active plane was passively shifted. Consequently, differently oriented slips were generated. In addition, the magnified view of the atomic configuration on the newly appeared surface between two HCP layers is shown in Figure 15(f), where the closest configuration of the {111} plane is exhibited.

Figure 16 shows the stress variation for various models. Here, the asterisk (*) indicates that the deformation mode is a slide type as shown in Figure 14, whereas its absence indicates a bent type as in Figure 13. No specific difference in the stress variation was found even though the elastic modulus was dependent on the crystal

orientation.

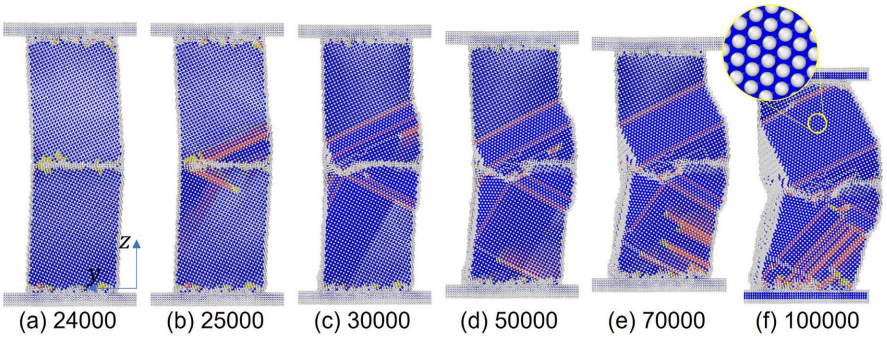

Figure 15. Atomic configuration under compression for lateral symmetric L70-70 bicrystal model from the 24,000th to 100,000th timesteps colored by CNA indicator.

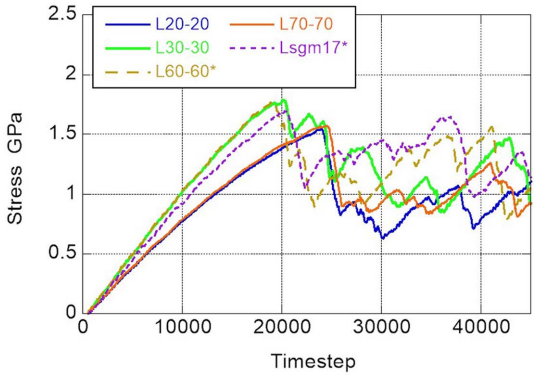

Figure 16. Stress variation for symmetric lateral grain-boundary models, where the * mark in the legend indicates that the deformation mode is a slide type.

6. Conclusions

In this study, MD simulations were carried out to clarify the deformation mechanism of nanopillars. Following simulations for single-crystal models to confirm their basic behavior, bicrystal models were investigated. When the GB was parallel to the longitudinal axis of the pillar, deformation proceeded by the generation and motion of the slip planes in each region. In particular, when the two crystals had a symmetric orientation, the slip planes were also observed symmetrically. The overall pillar shape was maintained almost rectangle. In contrast, when the GB was perpendicular to the longitudinal axis, specific deformation was observed. When the upper-half region exhibited a high propensity for slip, the slip planes were generated primarily within the region. Consequently, the overall deformation of the pillar was also intense in the upper-half region, thereby causing the lower-half region to remain undeformed. In the symmetric models, two types of deformation modes were observed: bent and slide types.

In this study, the orientations of the FCC crystals were limited to those rotated around one axis; *i.e.*, only the tilt GBs were considered. Twist GB models will be targeted in our future research. In addition, the relative angle of the GB against

the pillar axis and the loading direction will also be investigated. Based on these research directions, a more detailed investigation of the deformation mechanism, including the slip and dislocation behavior and the influence of GBs will be performed. The nanopillar model presented in this study provides an effective foundation for future work, leading to advanced technology utilizing nanopillar structures.

Conflicts of Interest

The authors declare no conflicts of interest regarding the publication of this paper.

References

[1] Hawi, S., Goel, S., Kumar, V., Pearce, O., Ayre, W.N. and Ivanova, E.P. (2022) Critical Review of Nanopillar-Based Mechanobactericidal Systems. *ACS Applied Nano Materials*, **5**, 1-17. https://doi.org/10.1021/acsanm.1c03045

[2] Jenkins, J., Mantell, J., Neal, C., Gholinia, A., Verkade, P., Nobbs, A.H., *et al.* (2020) Antibacterial Effects of Nanopillar Surfaces Are Mediated by Cell Impedance, Penetration and Induction of Oxidative Stress. *Nature Communications*, **11**, Article No. 1626. https://doi.org/10.1038/s41467-020-15471-x

[3] Mariani, G., Scofield, A.C., Hung, C.-H. and Huffaker, D.L. (2013) Gaas Nanopillar-Array Solar Cells Employing *in Situ* Surface Passivation. *Nature Communications*, **4**, Article No. 1497. https://doi.org/10.1038/ncomms2509

[4] Kapadia, R., Fan, Z., Takei, K. and Javey, A. (2012) Nanopillar Photovoltaics: Materials, Processes, and Devices. *Nano Energy*, **1**, 132-144. https://doi.org/10.1016/j.nanoen.2011.11.002

[5] Dolores-Calzadilla, V., Romeira, B., Pagliano, F., Birindelli, S., Higuera-Rodriguez, A., van Veldhoven, P.J., *et al.* (2017) Waveguide-Coupled Nanopillar Metal-Cavity Light-Emitting Diodes on Silicon. *Nature Communications*, **8**, Article No. 14323. https://doi.org/10.1038/ncomms14323

[6] Nimaga, O.G., He, B.B., Cheng, G.J., Yen, H.W. and Huang, M.X. (2019) Revealing Orientation-Dependent Martensitic Transformation in a Medium Mn Steel by Micropillar Compression. *International Journal of Plasticity*, **123**, 165-177. https://doi.org/10.1016/j.ijplas.2019.07.016

[7] Peng, S., Jin, K., Yi, X., Dong, Z., Guo, X., Liu, Y., *et al.* (2022) Mechanical Behavior of the HfNbZrTi High Entropy Alloy after Ion Irradiation Based on Micro-Pillar Compression Tests. *Journal of Alloys and Compounds*, **892**, Article ID: 162043. https://doi.org/10.1016/j.jallcom.2021.162043

[8] Zhang, Q., Huang, R., Jiang, J., Cao, T., Zeng, Y., Li, J., *et al.* (2022) Size Effects and Plastic Deformation Mechanisms in Single-Crystalline CoCrFeNi Micro/Nanopillars. *Journal of the Mechanics and Physics of Solids*, **162**, Article ID: 104853. https://doi.org/10.1016/j.jmps.2022.104853

[9] Kunz, A., Pathak, S. and Greer, J.R. (2011) Size Effects in Al Nanopillars: Single Crystalline vs. Bicrystalline. *Acta Materialia*, **59**, 4416-4424. https://doi.org/10.1016/j.actamat.2011.03.065

[10] Kim, Y., Lee, S., Jeon, J.B., Kim, Y., Lee, B., Oh, S.H., *et al.* (2015) Effect of a High Angle Grain Boundary on Deformation Behavior of Al Nanopillars. *Scripta Materialia*, **107**, 5-9. https://doi.org/10.1016/j.scriptamat.2015.05.005

[11] Xu, S., Guo, Y.F. and Ngan, A.H.W. (2013) A Molecular Dynamics Study on the Ori-

entation, Size, and Dislocation Confinement Effects on the Plastic Deformation of Al Nanopillars. *International Journal of Plasticity*, **43**, 116-127. https://doi.org/10.1016/j.ijplas.2012.11.002

[12] Healy, C.J. and Ackland, G.J. (2014) Molecular Dynamics Simulations of Compression-Tension Asymmetry in Plasticity of Fe Nanopillars. *Acta Materialia*, **70**, 105-112. https://doi.org/10.1016/j.actamat.2014.02.021

[13] Xu, S., Startt, J.K., Payne, T.G., Deo, C.S. and McDowell, D.L. (2017) Size-Dependent Plastic Deformation of Twinned Nanopillars in Body-Centered Cubic Tungsten. *Journal of Applied Physics*, **121**, Article ID: 175101. https://doi.org/10.1063/1.4982754

[14] Lee, J.S., Xu, G., Suh, J.S., Bae, J.H., Suh, B., Kim, Y.M., *et al.* (2024) Atomistic Investigation into the Formation of Axial Weak Twins during the Compression of Single-Crystal Mg Nanopillars. *Acta Materialia*, **263**, Article ID: 119512. https://doi.org/10.1016/j.actamat.2023.119512

[15] Zhang, J., Zhang, M., Deng, L., Jin, J., Gong, P. and Wang, X. (2020) Mechanical Behavior of Tetragonal Zirconia Nanopillars Subjected to Uniaxial Loading: A Molecular Dynamics Study. *Mechanics of Materials*, **151**, Article ID: 103666. https://doi.org/10.1016/j.mechmat.2020.103666

[16] Regan, B., Aghajamali, A., Froech, J., Tran, T.T., Scott, J., Bishop, J., *et al.* (2020) Plastic Deformation of Single-Crystal Diamond Nanopillars. *Advanced Materials*, **32**, Article ID: 1906458. https://doi.org/10.1002/adma.201906458

[17] Shigihara, Y. (2025) Compression Simulation of Al Bicrystal Nanopillars Using Molecular Dynamics Method. Master's Thesis, Department of Mechanical Systems Engineering, Yamagata University. (In Japanese)

[18] Thompson, A.P., Aktulga, H.M., Berger, R., Bolintineanu, D.S., Brown, W.M., Crozier, P.S., *et al.* (2022) LAMMPS—A Flexible Simulation Tool for Particle-Based Materials Modeling at the Atomic, Meso, and Continuum Scales. *Computer Physics Communications*, **271**, Article ID: 108171. https://doi.org/10.1016/j.cpc.2021.108171

[19] Zhou, X.W., Wadley, H.N.G., Johnson, R.A., Larson, D.J., Tabat, N., Cerezo, A., *et al.* (2001) Atomic Scale Structure of Sputtered Metal Multilayers. *Acta Materialia*, **49**, 4005-4015. https://doi.org/10.1016/s1359-6454(01)00287-7

[20] Stukowski, A. (2009) Visualization and Analysis of Atomistic Simulation Data with OVITO—The Open Visualization Tool. *Modelling and Simulation in Materials Science and Engineering*, **18**, Article ID: 015012. https://doi.org/10.1088/0965-0393/18/1/015012

[21] Honeycutt, J.D. and Andersen, H.C. (1987) Molecular Dynamics Study of Melting and Freezing of Small Lennard-Jones Clusters. *The Journal of Physical Chemistry*, **91**, 4950-4963. https://doi.org/10.1021/j100303a014

[22] Kelchner, C.L., Plimpton, S.J. and Hamilton, J.C. (1998) Dislocation Nucleation and Defect Structure during Surface Indentation. *Physical Review B*, **58**, 11085-11088. https://doi.org/10.1103/physrevb.58.11085